Article

Analysis of the Radiation Attenuation Parameters of Cu$_2$HgI$_4$, Ag$_2$HgI$_4$, and (Cu/Ag/Hg I) Semiconductor Compounds

Heba Y. Zahran [1,2,*], El Sayed Yousef [1,3], Mohammed S. Alqahtani [4], Manuela Reben [5], Hamed Algarni [1], Ahmad Umar [6,7], Hasan B. Albargi [6,8], Ibrahim S. Yahia [1,2,3] and Nehal Sabry [2]

[1] Laboratory of Nano-Smart Materials for Science and Technology (LNSMST), Department of Physics, Faculty of Science, King Khalid University, P.O. Box 9004, Abha 61413, Saudi Arabia; omn_yousef2000@yahoo.com (E.S.Y.); halgarni@kku.edu.sa (H.A.); dr_isyahia@yahoo.com (I.S.Y.)

[2] Nanoscience Laboratory for Environmental and Bio-Medical Applications (NLEBA), Metallurgical Lab.1, Semiconductor Lab., Nuclear Lab., Department of Physics, Faculty of Education, Ain Shams University, Roxy, Cairo 11757, Egypt; na_sabry@hotmail.com

[3] Research Center for Advanced Materials Science (RCAMS), King Khalid University, P.O. Box 9004, Abha 61413, Saudi Arabia

[4] Department of Radiological Sciences, College of Applied Medical Sciences, King Khalid University, P.O. Box 9004, Abha 61421, Saudi Arabia; mosalqhtani@kku.edu.sa

[5] Faculty of Materials Science and Ceramics, AGH—University of Science and Technology, al. Mickiewicza 30, 30-059 Cracow, Poland; manuelar@agh.edu.pl

[6] Department of Physics, Faculty of Science and Arts, Najran University, P.O. Box 1988, Najran 11001, Saudi Arabia; ahmadumaresn@gmail.com (A.U.); hbalbargi@nu.edu.sa (H.B.A.)

[7] Promising Centre for Sensors and Electronic Devices (PCSED), Najran University, P.O. Box 1988, Najran 11001, Saudi Arabia

[8] Department of Chemistry, Faculty of Science and Arts, Najran University, P.O. Box 1988, Najran 11001, Saudi Arabia

* Correspondence: heldemardash@kku.edu.sa

Abstract: This analysis aims to determine photon attenuation for five different ternary and binary iodide compounds using Phy-X/PSD software. For a broad range of photon energies between 0.015 and 15 MeV, the mass attenuation coefficient (MAC), linear attenuation coefficient (LAC), half-value layer (HVL), tenth-value layer (TVL), and mean free path (MFP) for the samples of Cu$_2$HgI$_4$, Ag$_2$HgI$_4$, CuI, AgI, and HgI were calculated. For illustration, the following values of TVL apply at 1 MeV: S1: 6.062 cm, S2: 6.209 cm, S3: 6.929 cm, S4: 6.897 cm, and S5: 4.568 cm. Some important parameters, such as total atomic cross-sections (ACS), electronic cross-sections (ECS), the effective atomic numbers (Zeff), effective electron density (Neff), and effective conductivity (Ceff) of the samples were also calculated. Additionally, exposure buildup factors (EBF) and energy-absorption buildup factor (EABF) were estimated. These data on the radiation characteristics of our samples could be useful for gamma attenuation. The HgI sample has the highest FNRCS values (0.0892) relative to the other tested samples showing good neutron attenuation features. The CuI sample shows low gamma attenuation features; in contrast, it shows high neutron attenuation features.

Keywords: Cu$_2$HgI$_4$; Ag$_2$HgI$_4$; semiconductor compounds; gamma-ray attenuation; fast neutron removal cross-section; build-up factors; Z_{eff}

1. Introduction

Ionizing radiation has adverse impacts on the human body in laboratories, hospitals, and nuclear power plants, so radiation protectors attract considerable attention from researchers. The concept of radiation shielding is dependent on a medium's ability to reduce the impact of photons by attenuating them. So, research on the relationship between radiation and matter requires a proper characterization and evaluation of penetration and radiation diffusion in a medium [1]. The attenuation coefficient can calculate the

probability of possible interactions between gamma rays and atomic nuclei. The *MAC*, mass attenuation coefficient, accurate values are required to produce key data in various fields such as dosimeter protection, radiation shielding, nuclear diagnostic and medicine, and other applications [2,3]. Half value (*HVL*), mean free path (*MFP*), effective nuclear number (Z_{eff}), effective electron density (N_{eff}), and effective conductivity (C_{eff}) are also important quantities required to know the gamma-ray penetration [2,4]. Detecting photon buildup factors is critical for determining a defensive material's effectiveness [4]. The exposure buildup *(EBF)* and energy absorption buildup factors (*EABF*) are the two types of buildup factors defined in detail by the American Nuclear Society (ANSI/ANS) [5–7].

Preserving the environment from gamma radiation is most often achieved with lead and concrete [4]. However, the toxicity of lead and its low melting point have limited its use in nuclear applications [2]. Concrete also has limitations in its use as a shield due to its immovability and the generation of cracks in structures over time [8–10]. Thus, researchers focused on creating new radiation protection materials with desirable properties. For testing materials attenuation characteristics of various chemical compositions at various gamma-ray and neutron energies, theoretical methods (e.g., WinXCOM [11], FLUKA [12], PENELOPE [13], MCNPX [14], Phy-X/PSD [15]) are promising and simple pre-experiment methods. Several researchers have used Phy-X/PSD, a new free online program created by Sakar et al. [15] to measure essential photon-attenuation parameters accurately. Imen Kebaili et al. [16] studied gamma-ray shielding properties of lead borovanadate glasses using Phy-X/PSD. A. M. S. Alhuthali et al. [17] used Phy-X/PSD software to study the radiation attenuation properties of P_2O_5-SiO_2-K_2O-MgO-CaO-MoO_3 glasses. Additionally, Phy-X/PSD Software by İ. Akkurt and H.O. Tekin was used to study radiological parameters for bismuth oxide glasses [18].

The current research focuses on investigating five different ternary and binary iodide compounds (Cu_2HgI_4, Ag_2HgI_4, CuI, AgI, and HgI) radiation attenuation features for gamma rays and neutrons by using Phy-X/PSD software. We select our samples based on desired melting point and density characteristics. The two ternary samples Cu_2HgI_4 and Ag_2HgI_4 densities are 6.2 and 6.07 g/cm^3, respectively. CuI density is 5.67 g/cm^3, and its melting point is 595 °C [19]. The melting point of AgI is 558 °C, and its density is 5.68 g/cm^3. [19]. The high density and high atomic number elements of mercury iodide HgI are (7.7 g/cm^3) and (Z_{Hg} = 80 and Z_I = 53). Many important properties make mercury iodide (HgI_2) technologically attractive as a room temperature radiation detector [20].

For testing the sample's ability to attenuate gamma-rays in the photon energy range (0.015–15 MeV), radiation protection parameters including *MAC, MFP, HVL*, Z_{eff}, N_{eff}, and C_{eff} have been investigated. Total atomic cross-sections (*ACS*), electronic cross-sections (*ECS*), and photon buildup factors values were measured at the same energies. In addition, the *FNRCS* (fast neutron removal cross-section) is measured [15] and compared to concrete and commercial glasses. The calculated data provides information necessary for a particular energy attenuation of chosen compounds for the indirect ionizing radiation.

2. Materials and Methods

2.1. The Phy-X/PSD Online Software

Two ternary compounds Cu_2HgI_4 and Ag_2HgI_4 (coded as S1 and S2, respectively) and three different binary compounds CuI (coded as S3), AgI (coded as S4) and HgI (coded as S5) over a wide photon energy range from 0.015 to15 MeV have been examined as radiation attenuators by using Phy-X/PSD. The remote server, which possesses Intel(R) Core(TM) i7-2600 CPU @ 3.40 GHz CPU with 1 GB installed memory, is (Phy-X/PSD) a recent software developed by Sakar et al. [15]. Such software can estimate several radiation attenuation parameters at a wide range of energy. It is written in NodeJS v8.4.0, serving with Nginx 1.15.8. Security among server and client browsers is established through 256 Bit Positive SSL. This software with additional information can be found on the web page of https://phy-x.net/PSD.

2.2. Theoretical Basis

For monoenergetic photon beam with initial intensity I_o moving across x (cm) sample thickness, the beam intensity will be decreased to an intensity I, and the photon beam attenuation can be calculated as follows [21]:

$$I = I_o\, e^{-\mu x} \tag{1}$$

where μ refers to the linear attenuation coefficient. The mass attenuation coefficient (*MAC*) offers useful information on materials as radiation attenuators. The following equation determines *MAC* for compound and mixture [22]:

$$\left(\frac{u}{\rho}\right) = \sum_i w_i\, (u/\rho)_i, \tag{2}$$

where μ/ρ refers to the mass attenuation coefficient value and w_i refers to the weight fraction of ith element in the material. The *LAC* parameter is needed to calculate the required magnitudes to reduce initial irradiation to half or tenth times its original strength. The half-value layer (*HVL*) can be calculated to minimize the strength of photons by half, as follows [23]:

$$HVL = \frac{ln2}{\mu}, \tag{3}$$

Ninety percent of the incident light can be blocked through the tenth value layer (*TVL*) that can be calculated as follows [24]:

$$TVL = \frac{ln10}{\mu} \tag{4}$$

The mean free path (*MFP*) refers to the mean distance that the photon traveled without interacting with the attenuator that can be measured from Equation (5) [25]:

$$MFP = \frac{1}{\mu}, \tag{5}$$

The effective atomic number Z_{eff} and electron density N_{eff} are essential material analysis parameters for radiation attenuators. The atomic cross-section (*ACS* (σ_a)) and the electronic cross-section (*ECS* (σ_e)) are first estimated to obtain the effective atomic number (Z_{eff}). Then, the interaction probability per atom in the unit volume of any material (*ACS*) can be calculated from the following equation [26]:

$$ACS = \sigma_a = \sigma_m \frac{1}{\sum_i n_i} = (u/\rho)_{target} / N_A \sum_i \frac{w_i}{A_i} \tag{6}$$

where σ_m, A_i, w_i, and N_A are the molecular cross-section, the atomic weight, the fractional weight for each component in the target, and Avogadro's constant. Additionally, the interaction probability per electron in the unit volume of any substance (*ECS*) can be calculated as follows [27]:

$$ECS = \sigma_e = \frac{1}{N_A} \sum_i \left(\frac{u}{\rho}\right)_i \frac{f_i A_i}{z_i} \tag{7}$$

where the atomic number Z_i and the fractional abundance of the target individual elements f_i. To determine Z_{eff}, we can divide Equations (6) and (7) [28]:

$$Z_{eff} = \frac{\sigma_a}{\sigma_e}, \tag{8}$$

The electron density (N_{eff}) describes the interacting electrons per unit mass in the target; N_{eff} can be obtained from the next equation [29]:

$$N_{eff} = N \frac{Z_{eff}}{\sum_i f_i A_i},$$

(9)

Effective conductivity (C_{eff}) is one of the key parameters in photon matter interactions. This parameter is based on the number of free electrons created in the unit volume of the substance with the photon energy interacting. The effective conductivity (C_{eff}) can be estimated by this equation [30]:

$$C_{eff} = \left(\frac{N_{eff} \, \rho \, e^2 \, \tau}{m_e} \right) 10^3,$$

(10)

where ρ material's physical density, N_{eff} the effective electron density, e, and m are the electron charge in coulomb and the electron mass in kg. τ is the average electron lifetime (relaxation time) at the Fermi surface which can be estimated by the following formula [31]:

$$\tau = \frac{h}{K_B T} = \frac{h}{2\pi K_B T},$$

(11)

where h is the Planck's constant in J.s, T is the temperature in Kelvin and K_B is the Boltzmann's constant in J/K. In radiation protection applications, build-up factors are important to show the probability of photon dispersion. To determine the build-up factors, we have to measure two parameters, R and Z_{eq}. For example, the following equation can represent R at certain energy [32]:

$$R = \frac{\left(\frac{\mu}{\rho} \right)_{Com}}{\left(\frac{\mu}{\rho} \right)_{Total}},$$

(12)

where $\left(\frac{\mu}{\rho} \right)_{Com}$ is the Compton mass attenuation coefficient and $\left(\frac{\mu}{\rho} \right)_{Total}$ is the total mass attenuation for the material. Z_{eff} is a virtual atomic number representing the complex substance when photons are absorbed into materials, and this value is referred to as Z_{eq} when photons are scattered. The second important parameter for estimating the build-up factors (Z_{eq}) can be computed as follows [15]:

$$Z_{eq} = \frac{Z_1 (\log R_2 - \log R) + Z_2 (\log R - \log R_1)}{\log R_2 - \log R_1}$$

(13)

where R_1 and R_2 values denote $\left(\frac{\mu}{\rho} \right)_{Com} / \left(\frac{\mu}{\rho} \right)_{Total}$ for two elements with Z_1 and Z_2 atomic numbers. The buildup factors are classified into *EBF* and *EABF*, which refer to the exposure buildup factor and energy absorption buildup factor. Then, the Geometric Progression fitting (G-P) is applied to calculate the buildup factors. The fitting parameters for G-P can be detected as follows by revealing the R and Z_{eq} parameters [15]:

$$P = \frac{P_1 (\log Z_2 - \log Z_{eq}) + P_1 (\log Z_{eq} - \log Z_1)}{\log Z_2 - \log Z_1}$$

(14)

where P_1 and P_2 are the G-P-fitting parameters corresponding to the atomic numbers Z_1 and Z_2, respectively. Then *EABF* and *EBF* were evaluated by using G-P fitting through the following equations [15]:

$$B(E, X) = 1 + \frac{b-1}{K-1} (K^x - 1) \text{ for } K \neq 1, \ B(E, X) = 1 + (b-1)x \ K = 1,$$

(15)

where

$$K(E, X) = cx^a + d \frac{tanh\left(\frac{x}{Xk} - 2\right) - tanh(-2)}{1 - tanh\ (-2)} \text{ for } x \ \leq \ 40, \tag{16}$$

where E is the photon energy, x is penetration depth in mfp, and $K\ (E,X)$ is the dose-multiplicative factor.

3. Results and Discussions

3.1. Radiation Attenuation Parameters

The main gamma-ray attenuation parameters of the investigated samples were detected in the photon energy range from 0.015 to 15 MeV. In the stated energy range, photoelectric effect *PE*, Compton scattering *CS*, and pair production *PP* are predominant at three energy ranges [33–35]. The *MAC* values as a function of photon energy are shown in Figure 1. This Figure indicates that EPhoton < 100 keV represents the maximum MAC values for all the tested samples in the low-energy region. While viewing the HgI binary sample, one notices the highest *MAC* value. The tertiary samples (Cu_2HgI_4 and Ag_2HgI_4) obtained intermediate *MAC* values, while CuI and AgI binary samples obtained the lowest *MAC* values. For example, at 20 keV, The *MAC* values are 40.108, 35.897, 28.225, 22.183, and 59.615 cm^{-1} for S1, S2, S3, S4, and S5, respectively. Increasing the photon energy results in an exponential decrease in *MAC* values until the values stabilize [36]. For example at 0.6 MeV, The *MAC* values are 0.0911, 0.0909, 0.0808, 0.0824 and 0.106 cm^{-1} for Cu_2HgI_4, Ag_2HgI_4, CuI, AgI and HgI, respectively. As the photon energy increases, for the HgI binary sample, E_{Photon} > 1.02 MeV causes a small increase in *MAC* values.
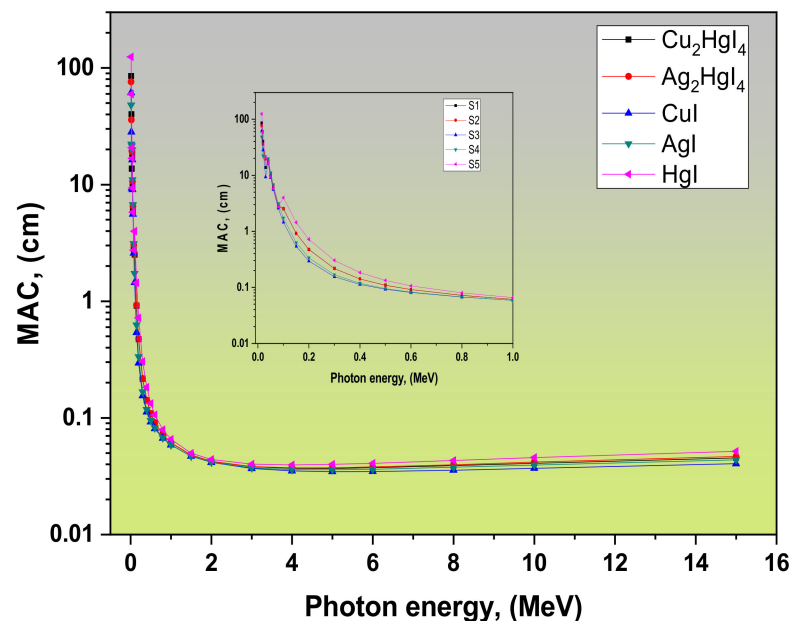

Figure 1. *MAC* of the tested samples versus photon energy.

The results obtained from Figure 1 may be related to the dominant presence of *PE* in the low-energy section. So, the cross-section for absorption is affected by the fourth or fifth power of atomic numbers (Z^{4or5}) of the sample atoms and the photon's energy as $1/E^{3.5}$ [37,38]. On the other hand, the cross-section diminishes exponentially with the energy and is proportional to Z in the intermediate energy range where the *CS* dominates [36]. In contrast, the cross-section is proportional to Z^2 in the highest energy range as the interaction of *PP* is dominant.

Figure 2 clarifies the *LAC* variations of the ternary compounds Cu_2HgI_4, Ag_2HgI_4, and three binary compounds CuI, AgI, and HgI as a function of photon energy ranges. The *LAC* values have the same behavior with photon energy as the *MAC*.
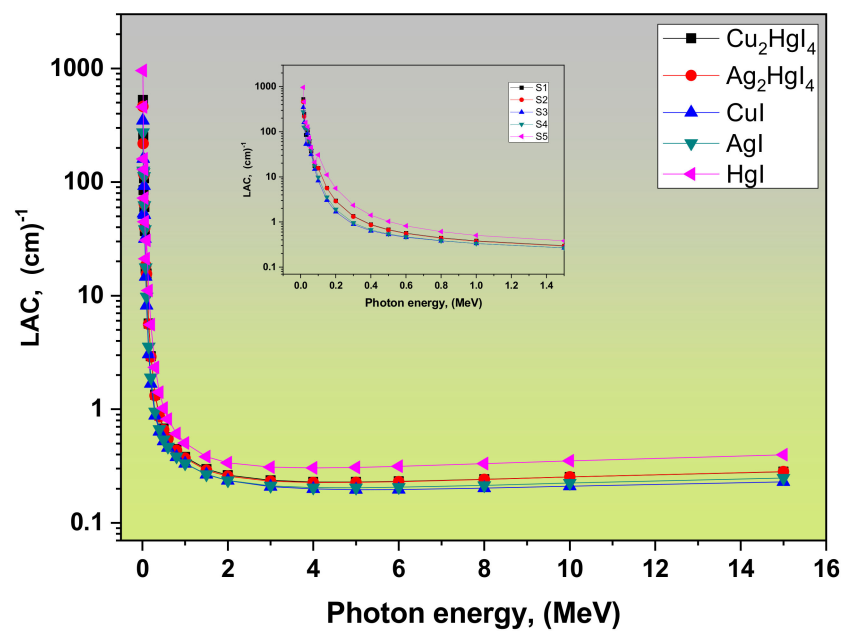
Figure 2. *LAC* of the tested samples versus photon energy.

In the selected energy range concerning the beam energy and the attenuator charge, as discussed in the previous graph, the *LAC* decreases quickly when the input energy is low but slows down as the input energy rises. It can also be seen from Figure 2 and Table 1 that the density of the samples primarily determines the *LAC* value. HgI (ρ = 7.7 g/cm^3) binary sample obtained the highest *LAC* value, the tertiary samples Cu$_2$HgI$_4$ (ρ = 6.2 g/cm^3) and Ag$_2$HgI$_4$ (ρ = 6.07 g/cm^3) obtained intermediate *LAC* values CuI (ρ = 5.67 g/cm^3) and AgI (ρ = 5.68 g/cm^3) binary samples obtained the lowest *LAC* values. Thus, the highest density sample HgI can absorb gamma photons more effectively for different medical and industrial applications.

Table 1. The density, MAC, and LAC for S1, S2, S3, S4, and S5 samples compared to concrete.

Refs.	LAC, (cm^{-1})		MAC, (cm^2/g)		Density r, (g/cm^3)	Samples
	5 MeV	1 MeV	5 MeV	1 MeV		
This work	0.229	0.38	0.037	0.061	6.2	Cu$_2$HgI$_4$ (S1)
	0.227	0.371	0.037	0.061	6.07	Ag$_2$HgI$_4$ (S2)
	0.196	0.332	0.035	0.059	5.67	CuI (S3)
	0.204	0.334	0.036	0.059	5.68	AgI (S4)
	0.308	0.504	0.04	0.065	7.7	HgI (S5)
[39]	0.0665	0.148	0.0289	0.064	2.3	Ordinary concrete
	0.0742	0.158	0.0297	0.063	2.5	Hematite-serpentine concrete
	0.0867	0.18	0.0299	0.062	2.9	Ilmenite-limonite concrete
	0.0894	0.192	0.0293	0.063	3.05	Basalt-magnetite concrete
	0.1036	0.215	0.0296	0.061	3.5	Ilmenite concrete
	0.1263	0.255	0.0316	0.064	4	Steel-scrap concrete
	0.1567	0.313	0.0307	0.061	5.11	Steel-magnetite concrete

Figure 3a represents the *HVL* variations of the ternary compounds Cu$_2$HgI$_4$, Ag$_2$HgI$_4$, and three binary compounds, CuI, AgI, and HgI, as a function of photon energy ranges. *HVL* magnitudes rise as the energy elevates in Figure 3a. The lowest levels for *HVL* have

been found at 15 keV, equal to 0.0013, 0.0015, 0.002, 0.0025, and 0.0007 cm for the samples from S1 to S5. In our previous work, at 15 KeV, *HVL* values equal 0.003, 0.002 and 0.002 for Cu_2MnGe [S, Se, Te]$_4$, respectively [40]. At 15.8 KeV, it equals 0.0021 cm for $CuInSe_2$ [41]. While their values at 15 MeV are 2.734, 2.734, 3.302, 3.092, and 1.968 cm for the five samples, respectively. Thus, the large compound thickness is meant to absorb high-energy photons. CuI sample has the highest value at the same amount of energy. However, HgI has the lowest value as the quality of a photon's interaction is enhanced by a denser sample rather than a lower density one.
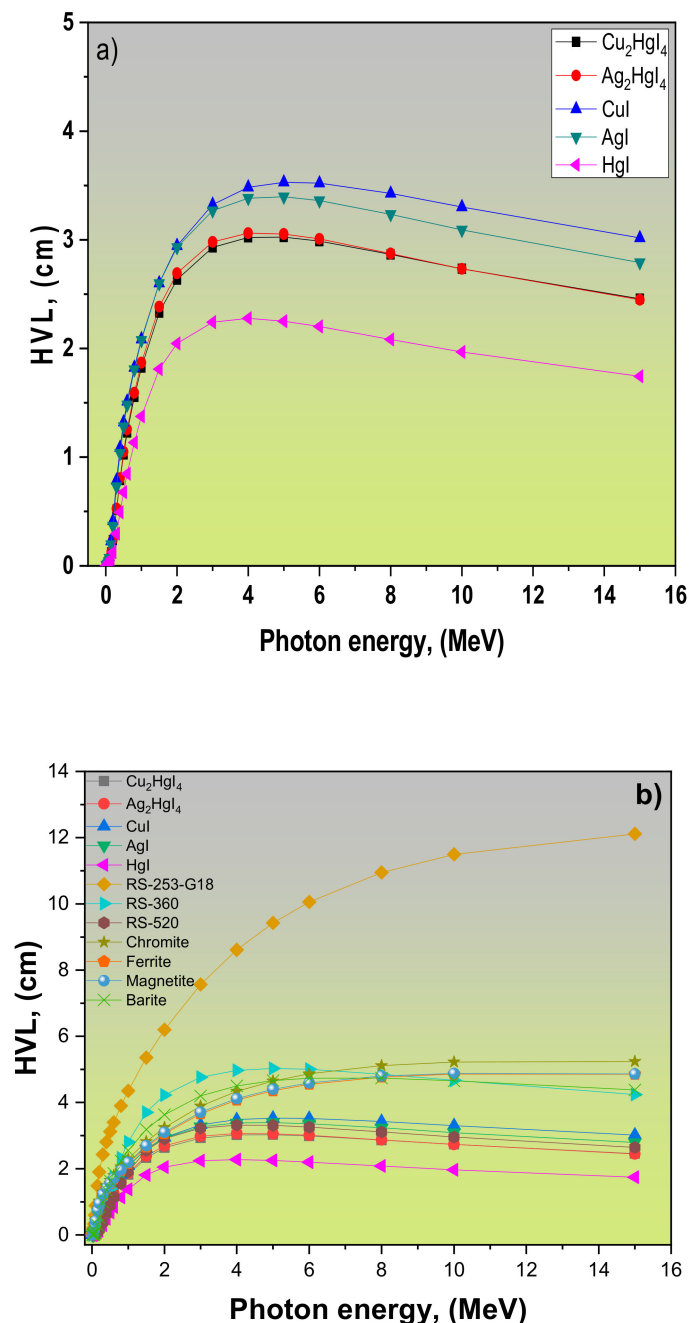
Figure 3. (**a**) *HVL* of the tested samples versus photon energy. (**b**) *HVL* of the tested samples versus photon energy compared with chromite, ferrite, magnetite, barite, and three commercial shielding glasses.

Figure 3b shows *HVL* results for the studied samples compared with chromite, ferrite, magnetite, barite [38,39], RS-520, RS-360, and RS-253-G18 [38,42], the three commercial

shielding glasses. As illustrated, all investigated samples have *HVL* values lower than the corresponding values of the other set of comparison samples. In addition, Cu_2HgI_4, Ag_2HgI_4, and HgI attain greater attenuation than other specimens because the quality of the attenuator means it has a lower *HVL*.

Figure 4 depicts the *TVL* values for various samples related to the selected photon energy range (0.15–15 MeV). Sample HgI has the lowest *TVL* value at the chosen energy values, so the sample density significantly impacts the *TVL*. As detected, the *TVL* values at 1 MeV are 6.062, 6.209, 6.929, 6.897, and 4.568 cm for the samples from S1 to S5. So, HgI is preferred practically because of has the best radiation attenuation efficiency.
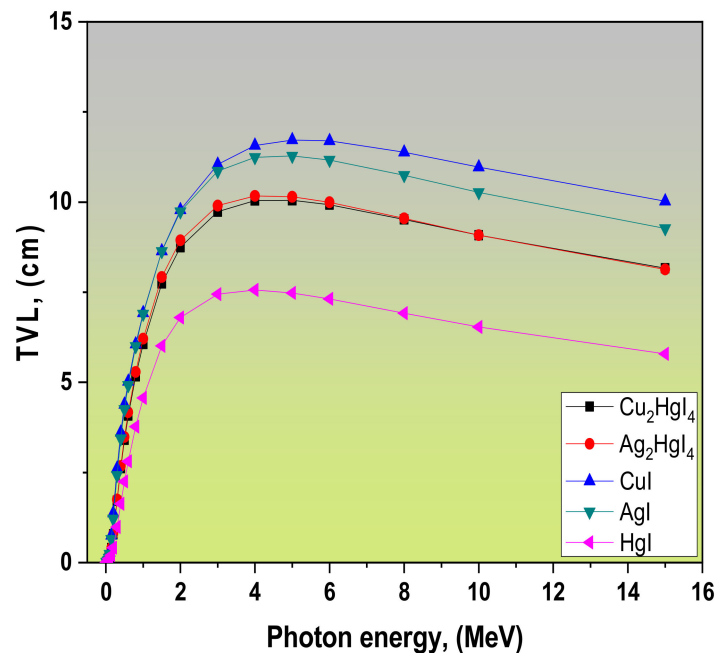

Figure 4. *TVL* of the tested samples versus photon energy.

The *mfp* values of the examined samples vary with the incident photon energy, as illustrated in Figure 5a. According to this Figure, the HgI sample has a lower *mfp* than other samples, indicating improved attenuation performance due to increased sample density. Additionally, one can notice that for all samples, the *mfp* values continuously increase with energy till nearly 6 MeV, then slightly decrease.

Figure 5b illustrates the comparison for the studied samples with some radiation shielding materials, namely chromite, ferrite, magnetite, barite, and the three commercial shielding glasses [38,39,42]. Similar to comparing the same radiation shielding materials with *HVL*, one can observe Cu_2HgI_4, Ag_2HgI_4, and HgI samples achieve better attenuation features than the comparable materials.

Figures 6 and 7 illustrate the *ACS* and *ECS* variations with photon energy. In Figures 6 and 7, one can note that sample CuI has the minimum values of both *ACS* and *ECS* at the same energy while HgI has the corresponding maximum values. The best attenuators are the materials with high *ACS* and *ECS* values. All the tested samples exhibit a decrease in the *ACS* and *ECS* values when energy increases. The *ECS* values are 8.03, 9.15, 4.70, 6.66 and 14.8×10^{-24} cm^2/g at 0.1 MeV then they decrease to 2.36, 2.39, 2.23, 2.29 and 2.62×10^{-25} cm^2/g at 1 MeV. A similar result had been observed in our previous work [40].

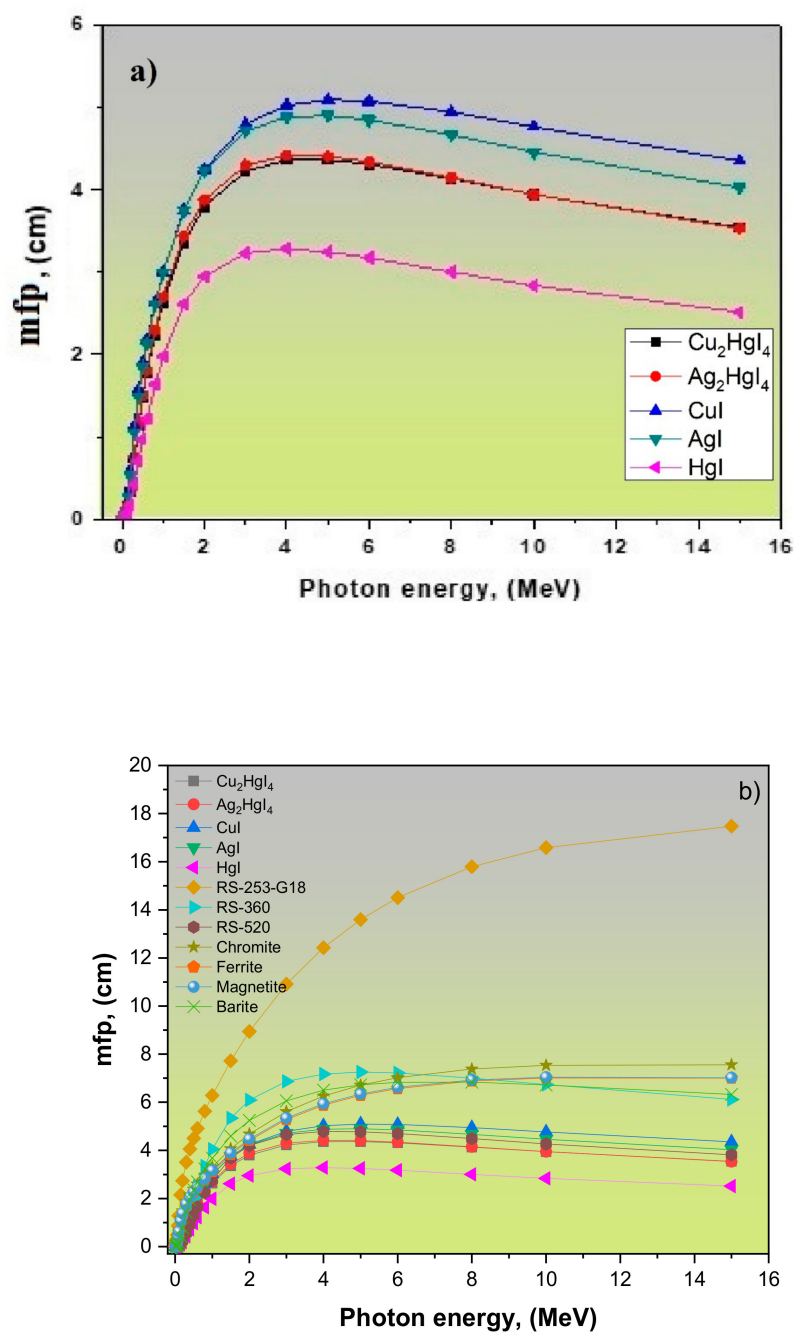**Figure 5.** (**a**) *mfp* of the tested samples versus photon energy. (**b**) *mfp* of the tested samples versus photon energy compared with chromite, ferrite, magnetite, barite, and three commercial shielding glasses.
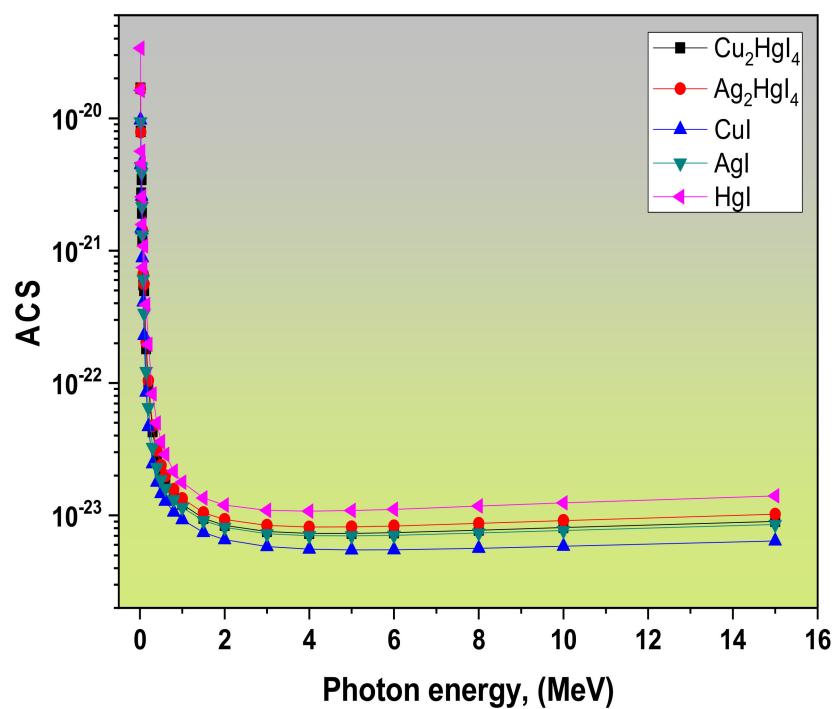
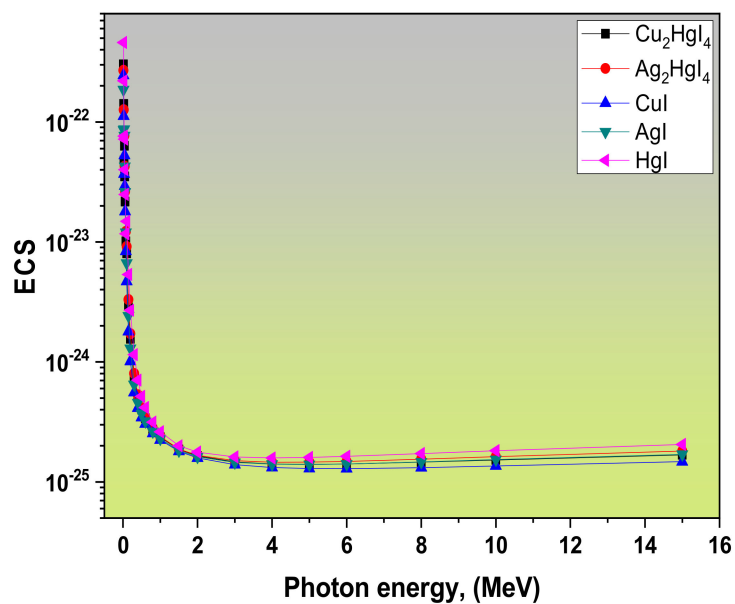**Figure 6.** *ACS* of the tested samples versus photon energy.

Figure 7. *ECS* of the tested samples versus photon energy.

Figure 8 shows the behavior of the Z_{eff} for all samples in the selected energy range 0.015–15 MeV. From Figure 8, generally, the Z_{eff} values rapidly diminish with photon energy rising and reaching a nearly constant value. The highest Z_{eff} values were found in the sample of HgI in all the analyzed energies.
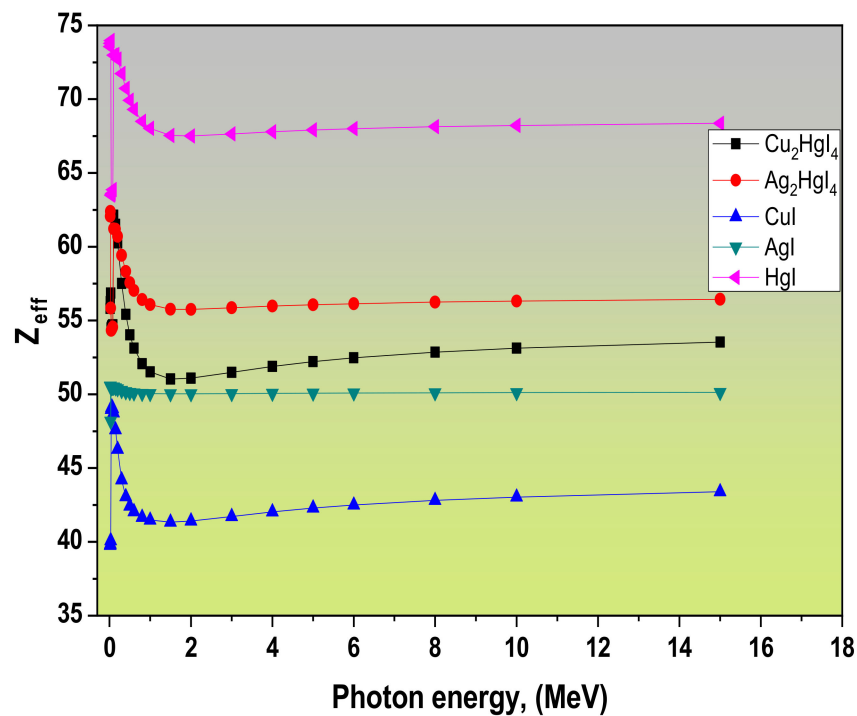
Figure 8. The Z_{eff} of the tested samples versus photon energy.

In Table 2, one can notice that CuI has maximum penetration of gamma photons while HgI has less penetration probability and more probability of interaction with gamma photons. Our samples have more probability of interaction than CdSe [43], Cu_2MnGeS_4, $Cu_2MnGeSe_4$ and $Cu_2MnGeTe_4$ [40] samples.

Table 2. The tested samples Z_{eff}, N_{eff} and C_{eff} values at 15 keV compared with corresponding values of Cu_2MnGe (S/Se/Te)$_4$ at 15 keV and Cd (Te/Se) at 14.8 keV.

Samples	Z_{eff}	N_{eff}	C_{eff}	Refs.
Cu_2HgI_4 (S1)	55.82	2.82×10^{23}	1.26×10^9	
Ag_2HgI_4 (S2)	62.07	2.83×10^{23}	1.24×10^9	
CuI (S3)	39.76	2.51×10^{23}	1.03×10^9	This work
AgI (S4)	50.54	2.59×10^{23}	1.06×10^9	
HgI (S5)	73.56	2.71×10^{23}	1.50×10^9	
CdTe	50.4	2.5×10^{23}	-	[43]
CdSe	39.2			
Cu_2MnGeS_4	27.13	3.41×10^{23}	1.01×10^9	
$Cu_2MnGeSe_4$	32.11	2.71×10^{23}	1.04×10^9	[40]
$Cu_2MnGeTe_4$	39.21	2.47×10^{23}	1.05×10^9	

Figure 9 illustrates N_{eff} changes for all examined specimens with photon energy in the selected range. From Figure 9, the N_{eff} trends are almost like the Z_{eff} trends in all compounds dependent on the photon energy.

The values of N_{eff} at 15 keV are illustrated in Table 2. Table 2 and Figure 9 clarify that sample HgI represents the lowest N_{eff} value. CuI sample has the highest corresponding value related to their inverse proportion to the average material atomic weight. All tested samples values are higher than the corresponding CdTe [43], CdSe [43] and $Cu_2MnGeTe_4$ [40] values and lower than Cu_2MnGeS_4 [40] value at nearly 15 keV. A similar result had been observed in our previous work [40].
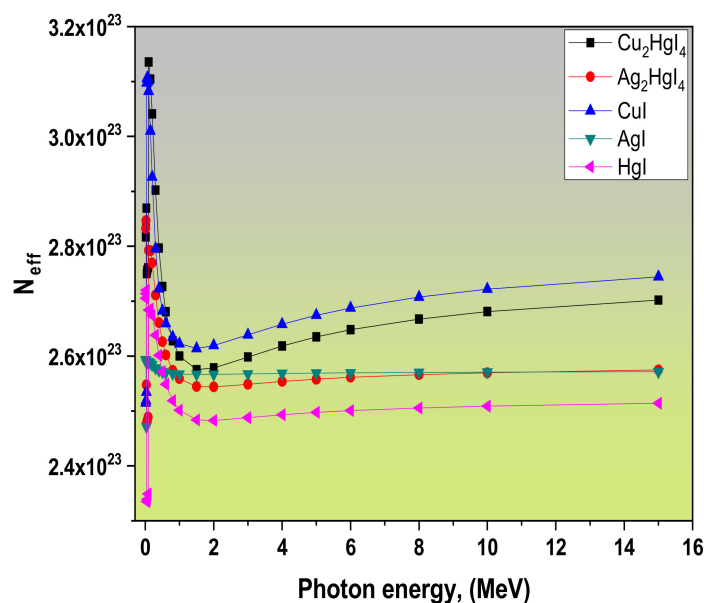
Figure 9. The N_{eff} of the tested samples versus photon energy.

The C_{eff} is another parameter that depends on the sample density, so its behavior with photon energy varies from that for N_{eff}. The C_{eff} values vary with photon energy, as shown in Figure 10, indicating that the higher free-electron generation in the PE region is than in other regions.
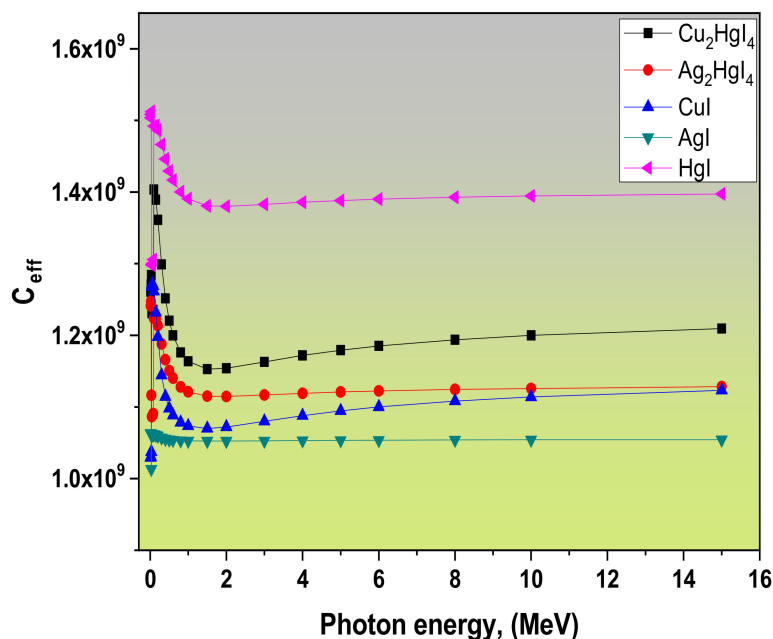

Figure 10. The C_{eff} of the tested samples versus photon energy.

Low-energy photons with longer wavelengths have more chances of interacting with the target material electrons. When the probability of this event rises, more electrons absorb photons, and more free electrons are formed. The values of C_{eff} at 15 keV are illustrated in Table 2. From Table 2, at low energy, the C_{eff} values of the HgI are higher than the other four samples. Except for CuI sample, our samples are higher than Cu_2MnGe $(S/Se/Te)_4$ values at 15 keV [40]. In the energy regions where CS is dominant, the C_{eff} values of the materials studied are almost photon energy independent. This behavior may be due to the

interaction probabilities with the target material electrons in the CS region are less than the PE region.

The variation of the *R* values within the examined energy range is shown in Figure 11. HgI has the minimum *R*-value at the same energy, and CuI has the corresponding maximum value. For example, *R* values at 0.8 MeV are 0.848, 0.849, 0.928, 0.914 and 0.752 for samples Cu_2HgI_4, Ag_2HgI_4, CuI, AgI and HgI respectively. Inelastic scattering is known as the variance of CS in the intermediate energy range. The R values for all samples reach a maximum at 1.5 MeV because the total cross-section is constant. The inelastic scattering reaches a maximum value within the selected range and is almost independent of the sample structure [2]. The *R* values at 1.5 MeV are 0.915, 0.914, 0.956, 0.948 and 0.859 for samples Cu_2HgI_4, Ag_2HgI_4, CuI, AgI and HgI respectively. As the energy rises, the dominance of PP elevates, and the CS probability begins to reduce, such that the *R* values start to decrease.
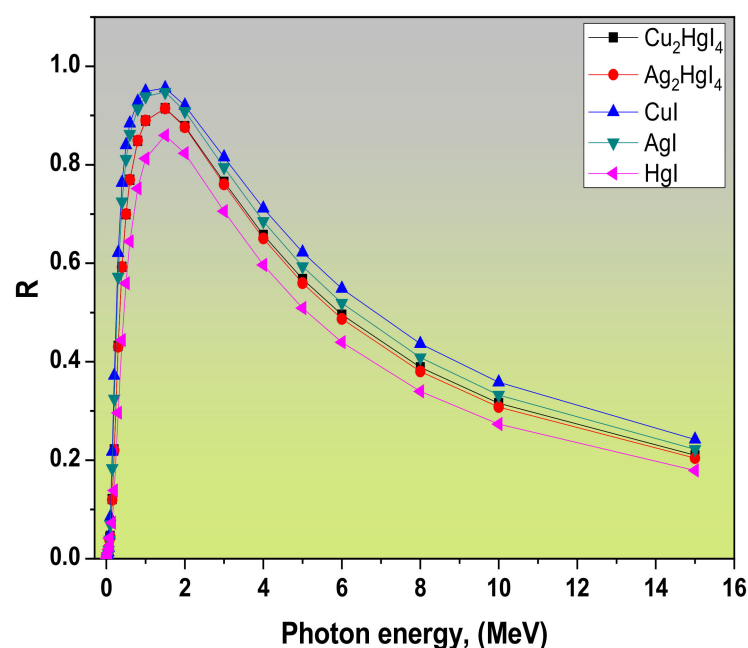

Figure 11. The variations of the $R((\mu/\rho_{Com})/(\mu/\rho_{Total}))$ ratio of the tested samples versus photon energy.

Figure 12 illustrates various Z_{eq} values of the tested samples over the studied energy range. The Z_{eq} values do not display significant energy-dependent variations for all samples. Additionally, it is observed that the Z_{eq} of photon energy is a partially similar trend as Z_{eff} of multi-element materials. A similar result had been observed in our previous work [40]. Furthermore, M. S. Al-Buriahi and B. T. Tonguc [44] reported that bismuth borate glasses exhibit this behavior.
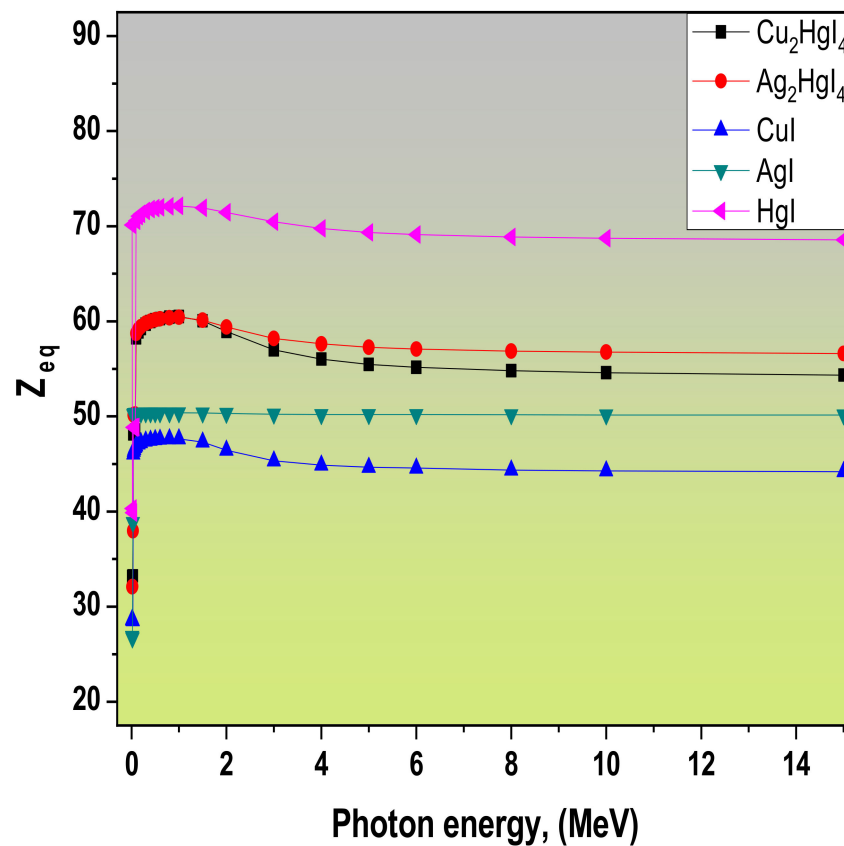
Figure 12. The Z_{eq} of the tested samples versus photon energy.

3.2. Dependence of EBF and EABF Values on the Photon Energy

Figures 13–17 represent the variations of *EBF* and *EABF* at 1, 5, 10, 15, 20, 25, 30, 35, and 40 *mfp* at the selected energy range for tested samples. The maxima of *EBF* and *EABF* are related to the energy range, penetration depth, and sample composition for all samples. With an increase in photon energy, *EBF* and *EABF* magnitudes increase to one or more peak values then decrease with further growth in photon energy. As PE is the predominant interaction in the low photon energy range, more photons can be absorbed, so the *EBF* and *EABF* reach the smallest. This observation was previously detected with Cu$_2$MnGe [S, Se, Te]$_4$ [40]. For photons with an intermediate energy region, the *EBF* and *EABF* reach the highest. This is due to the predominance of CS; photon energy is lost through scattering and cannot annihilate [45]. The photons have been reabsorbed in the high-energy range, as the predominant interaction is PP.
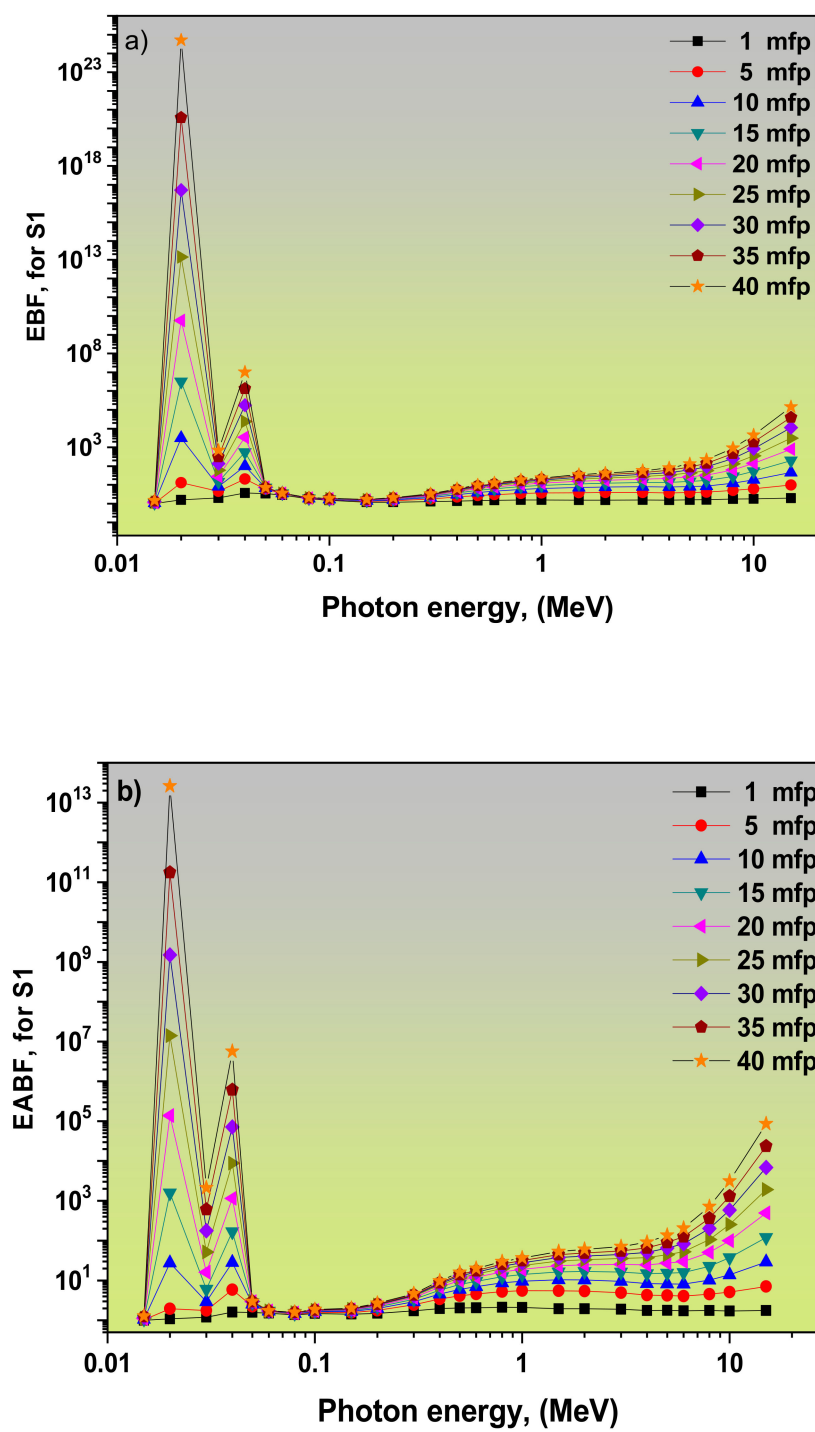
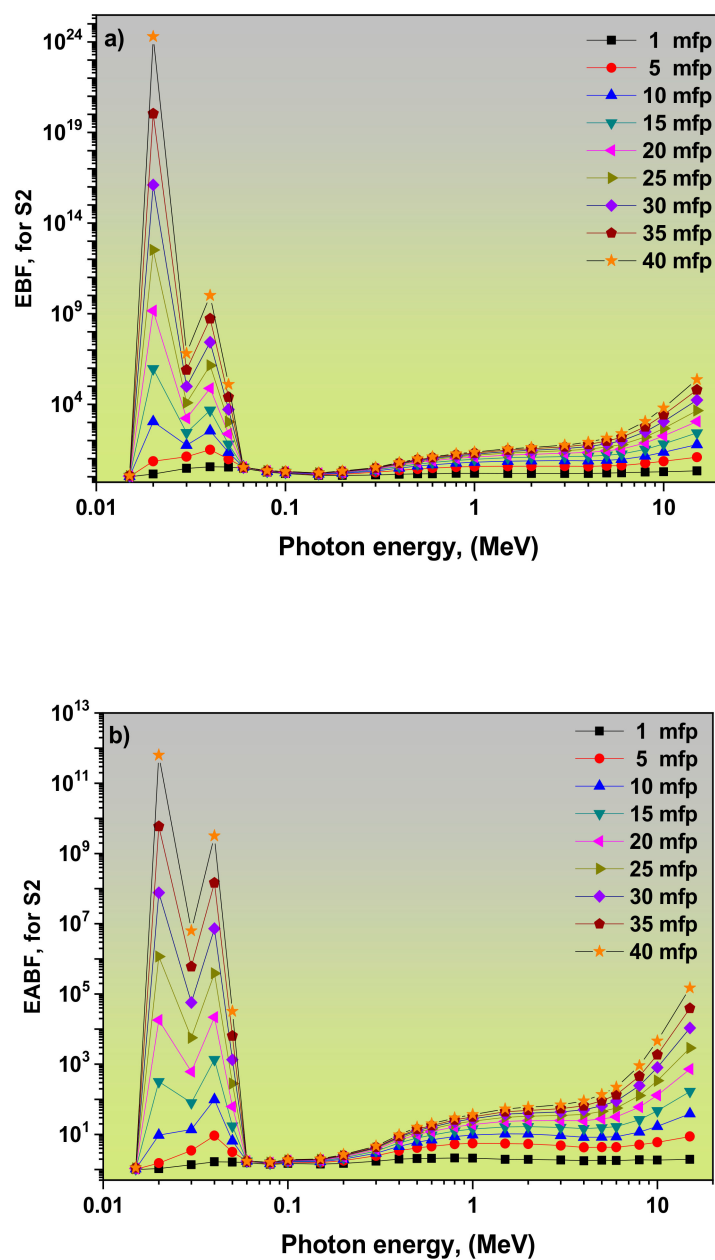**Figure 13.** The variations of (**a**) *EBF* and (**b**) *EABF* for Cu_2HgI_4 at different mfp versus photon energy.

Figure 14. The variations of (**a**) *EBF* and (**b**) *EABF* for Ag_2HgI_4 at different mfp versus photon energy.

Figure 15. The variations of (**a**) *EBF* and (**b**) *EABF* for CuI at different mfp versus photon energy.

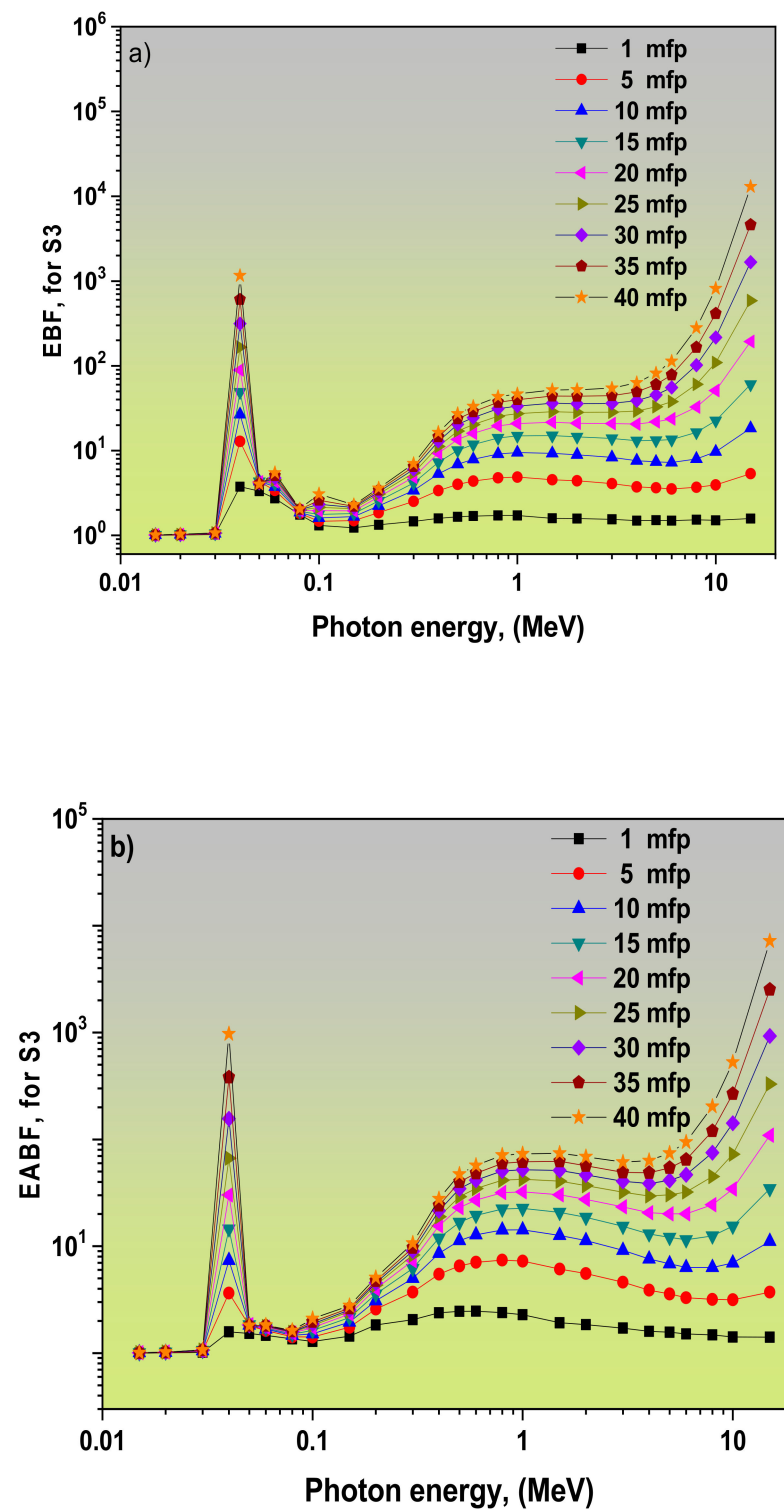**Figure 16.** Variations of (**a**) *EBF* and (**b**) *EABF* for AgI at different mfp versus photon energy.

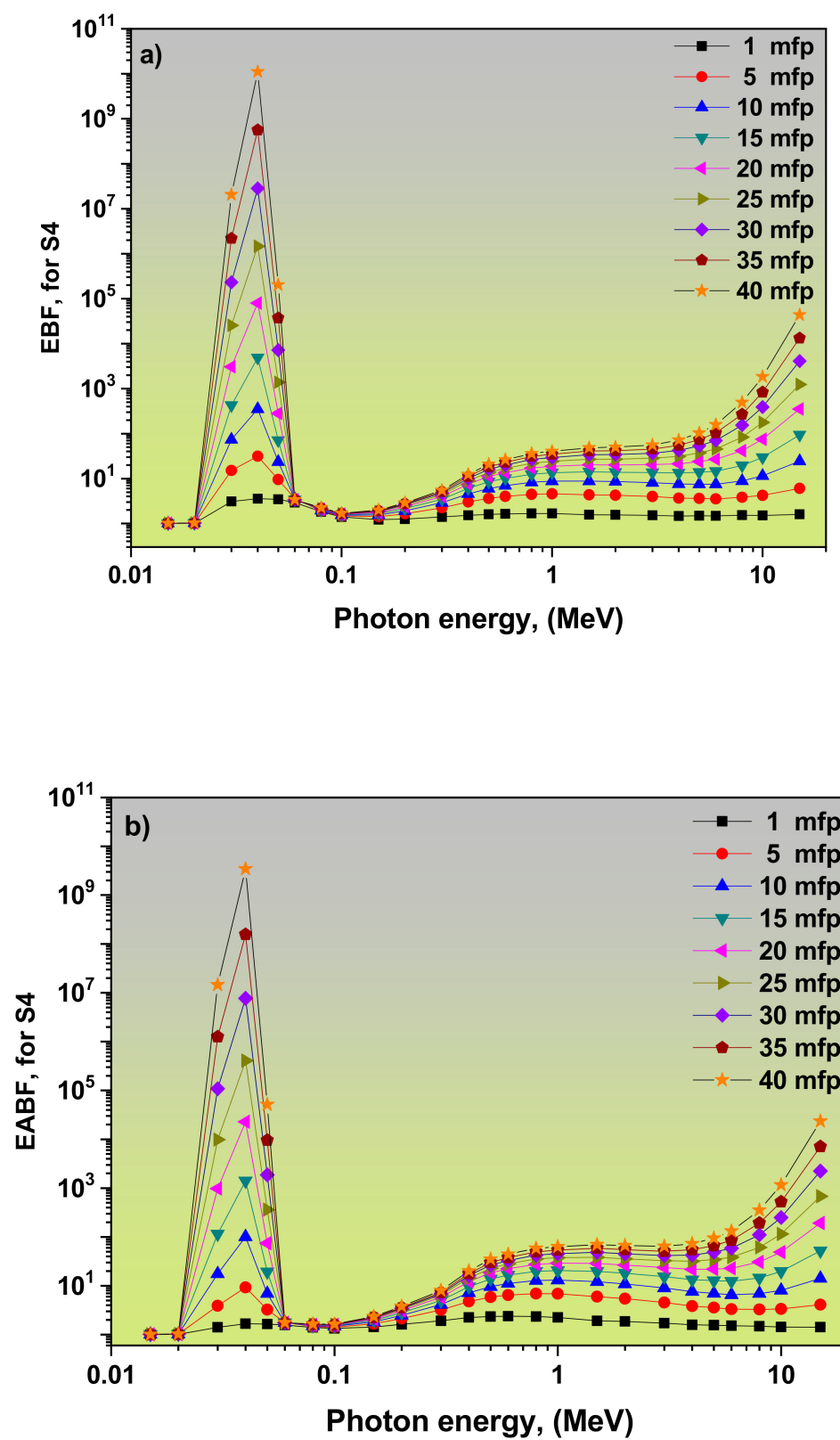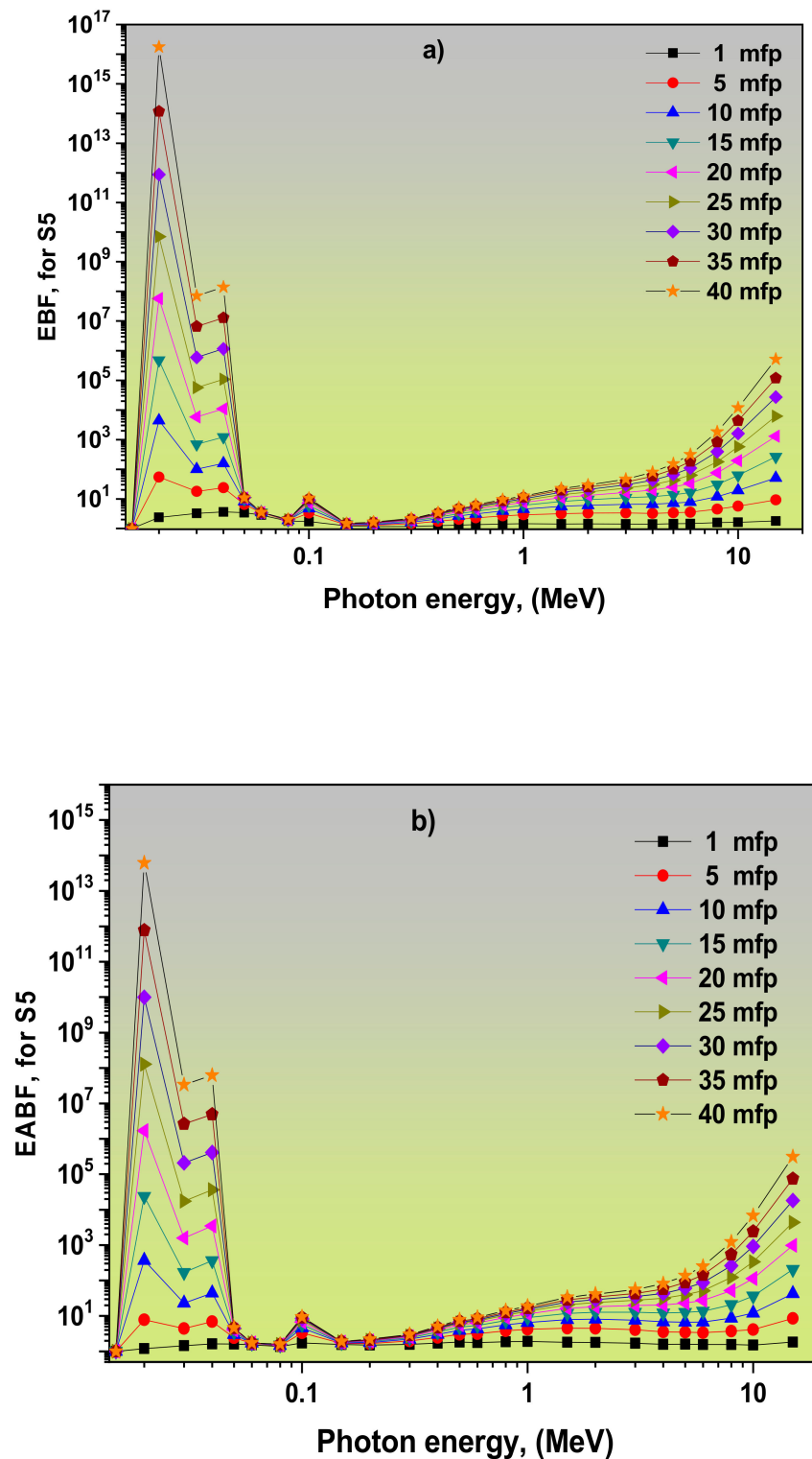**Figure 17.** The variations of (**a**) *EBF* and (**b**) *EABF* for HgI at different mfp versus photon energy.

Additionally, from Figures 13–17, at a penetration depth of 1 *mfp*, the *EBF* and *EABF* values are minimal. The highest corresponding values are observed at 40 *mfp* because multiple scatterings occur at high penetration depths [44]. *EABF* and *EBF* change differently with penetration depth at high energy (15 MeV) due to the pair production. Moreover, all samples reveal a sharp beak around 0.04 MeV due to the K-absorption edges of iodine ($\approx$33 keV) [46]. In Figure 13a,b, Figure 14a,b, and Figure 17a,b for Cu_2HgI_4, Ag_2HgI_4, and

HgI samples, respectively, there is another sharp beak around 0.02 MeV which *mfp* with the increment of *mfp* increase because of the L-absorption edges of Hg (Hg: 14.84) [47].

3.3. Fast Neutron Removal Cross-Section (FNRCS)

A helpful parameter for testing the attenuation of fast neutrons is the fast neutron removal cross-section *FNRCS* (Σ_R). It suggests that the neutrons could pass through the material without interacting. The equation to calculate Σ_R of a substance can be as follows [24,48]:

$$\frac{\Sigma_R}{\rho} = \sum_i W_i \left(\frac{\Sigma_R}{\rho} \right)_i, \tag{17}$$

where

$$W_i = \sum_i w_i \left(\rho \right)_s, \tag{18}$$

where $\left(\frac{\Sigma_R}{\rho} \right)_i$ represents the mass removal cross-section of the ith component; the partial density and the weight fraction of ith constituent are expressed as W_i and w_i. This quantity is represented as $(\rho)_s$ is the absorber density. *FNRCS* values for the 5 tested samples are 0.0833, 0.0783, 0.0854, 0.0779 and 0.0892 respectively. So, the HgI sample shows the highest neutron attenuation features relative to the other tested samples. Although the CuI sample has low photon radiation attenuation, it has a high neutron attenuation feature. The AgI sample has the lowest value of all tested samples, indicating fewer neutron attenuation features. Figure 18 compares *FNRCS* for the examined absorbers with some radiation shielding materials, namely chromite, ferrite, magnetite, barite, RS-520, RS-360, and RS-253-G18 [38,39,42]. Ferrite, magnetite, and chromite have the highest FNRCS values, as seen in Figure 18. The *FNRCS* value of HgI is higher than the corresponding values of RS-253-G18, RS-360, and RS-520. Cu_2HgI_4 and CuI values are higher than RS-360 and RS-520 values. So, HgI offers the best neutrons attenuation properties than the three commercial shielding glasses.
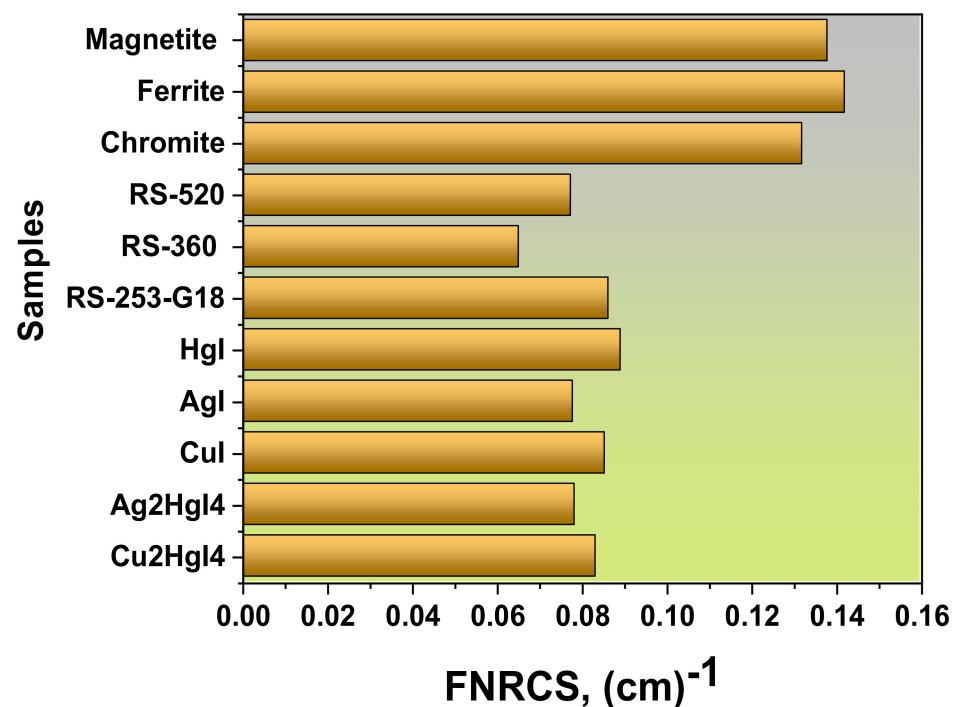

Figure 18. Comparison of FNRCS for the tested samples with chromite, ferrite, magnetite, barite, and three commercial shielding glasses.

4. Conclusions

The present work investigates the attenuation properties of γ-radiation, and fast neutrons for two ternary compounds, Cu_2HgI_4 and Ag_2HgI_4, coded as S1 and S2. Furthermore, three binary compounds CuI, AgI, and HgI coded as S3, S4, and S5, respectively, were investigated using Phy-X/PSD software with photon energy range from 0.015 to15 MeV. The results obtained represent that the HgI binary sample obtained the highest *MAC* and *LAC* values while CuI and AgI binary samples obtained the lowest corresponding values. So, the HgI sample (the highest density sample $\rho = 7.7$ g/cm^3) absorbs gamma photons more efficiently for the tested samples.

The HgI sample has a low *HVL* value varies between 0.0007–1.743 cm, while CuI has the highest values varies between 0.002–3.017 cm representing the higher attenuation features of HgI. All samples have *HVL* and *MFP* values lower than the corresponding values of chromite, ferrite, magnetite, barite, RS-360, and RS-253-G18. For all examined samples, *ACS* and *ECS* magnitudes diminish when energy increases. For instance, the *ECS* values are 8.03, 9.15, 4.70, 6.66 and 14.8 $\times$ 10^{-24} cm^2/g at 0.1 MeV and decrease to 2.36, 2.39, 2.23, 2.29 and 2.62 $\times$ 10^{-25} cm^2/g at 1 MeV.

The highest Z_{eff} and C_{eff} values obtained for the HgI sample represent that gamma photons have a higher chance of interacting and lower penetration probability. The obtained results show that the maxima of *EBF* and *EABF* are affected by the penetration depth, sample composition, and energy range. There is a sharp beak around 0.04 MeV for all samples due to the K-absorption edges of iodine ($\approx$33 keV). Concerning Cu_2HgI_4, Ag_2HgI_4, and HgI samples, there is another sharp beak around 0.02 MeV due to the L-absorption edges of Hg (Hg: 14.84)

FNRCS values for Cu_2HgI_4, Ag_2HgI_4, CuI, AgI and HgI are 0.0833, 0.0783, 0.0854, 0.0779 and 0.0892, respectively. So, HgI offers better neutrons attenuation characteristics than the other tested samples compared with the three commercial shielding glasses. The measured values represent that the HgI sample has good γ-rays and fast neutron attenuating features than other selected samples and can be used as a fast neutron protector and gamma-ray protector for technical and medical applications.

Author Contributions: H.Y.Z. performed data analysis and wrote and revised the whole manuscript. E.S.Y., M.S.A. and M.R. participated in calculations and data analysis. H.A., A.U. and H.B.A. reviewed the primary version and all calculations. I.S.Y. suggested the research idea and reviewed the final version. N.S. wrote the first version and performed data analysis. All authors have read and agreed to the published version of the manuscript.

Institutional Review Board Statement: Not applicable.

Informed Consent Statement: Not applicable.

Data Availability Statement: All original measurements and data analysis of this work will be available when required.

Conflicts of Interest: Authors confirm no conflict of interest.

References

1. Abdel-Rahman, W.; Podgorsak, E. Energy transfer and energy absorption in photon interactions with matter revisited: A step-by-step illustrated approach. *Radiat. Phys. Chem.* **2010**, *79*, 552–566. [CrossRef]
2. Alım, B. A comprehensive study on radiation shielding characteristics of Tin-Silver, Manganin-R, Hastelloy-B, Hastelloy-X and Dilver-P alloys. *Appl. Phys. A* **2020**, *126*, 1–19. [CrossRef]
3. Demir, D.; Turşucu, A. Studies on mass attenuation coefficient, mass energy absorption coefficient and kerma of some vitamins. *Ann. Nucl. Energy* **2012**, *48*, 17–20. [CrossRef]
4. Lakshminarayana, G.; Elmahroug, Y.; Kumar, A.; Dong, M.G.; Lee, D.-E.; Yoon, J.; Park, T. Li_2O–B_2O_3–Bi_2O_3 glasses: Gamma-rays and neutrons attenuation study using ParShield/WinXCOM program and Geant4 and Penelope codes. *Appl. Phys. A* **2020**, *126*, 1–16. [CrossRef]
5. White, G.R. The Penetration and Diffusion of Co60 Gamma-Rays in Water Using Spherical Geometry. *Phys. Rev.* **1950**, *80*, 154. [CrossRef]
6. Harima, Y. An historical review and current status of buildup factor calculations and applications. *Radiat. Phys. Chem.* **1993**, *41*, 631. [CrossRef]
7. American National Standard Institute. *Gamma-Ray Attenuation Coefficients and Buildup Factors for Engineering Materials*; Report ANSI/ANS-6.4.3-1991; American Nuclear Society: La Grange Park, IL, USA, 1991.
8. Abd-Allah, W.M.; Saudi, H.A.; Shaaban, K.S.; Farroh, H.A. Investigation of structural and radiation shielding properties of $40B_2O_3$–$30PbO$–(30-x) BaO-x ZnO glass system. *Appl. Phys. A* **2019**, *125*, 275. [CrossRef]
9. Kurudirek, M.; Chutithanapanon, N.; Laopaiboon, R.; Yenchai, C.; Bootjomchai, C. Effect of Bi_2O_3 on gamma ray shielding and structural properties of borosilicate glasses recycled from high pressure sodium lamp glass. *J. Alloy. Compd.* **2018**, *745*, 355–364. [CrossRef]
10. Lee, C.-M.; Lee, Y.H.; Lee, K.J. Cracking effect on gamma-ray shielding performance in concrete structure. *Prog. Nucl. Energy* **2007**, *49*, 303–312. [CrossRef]
11. Gerward, L.; Guilbert, N.; Jensen, K.; Levring, H. WinXCom—A program for calculating X-ray attenuation coefficients. *Radiat. Phys. Chem.* **2004**, *71*, 653–654. [CrossRef]
12. Battistoni, G.; Broggi, F.; Brugger, M.; Campanella, M.; Carboni, M.; Empl, A.; Fassò, A.; Gadioli, E.; Cerutti, F.; Ferrari, A.; et al. Applications of FLUKA Monte Carlo code for nuclear and accelerator physics. *Nucl. Instrum. Methods Phys. Res. Sect. B Beam Interact. Mater. Atoms* **2011**, *269*, 2850–2856. [CrossRef]
13. PENELOPE2014, A Code System for Monte-Carlo Simulation of Electron and Photon Transport. In Proceedings of the Workshop NEA-1525 PENELOPE2014, Barcelona, Spain, 29 June–3 July 2015.
14. Waters, L.S.; McKinney, G.W.; Durkee, J.W.; Fensin, M.; Hendricks, J.S.; James, M.R.; Johns, R.C.; Pelowitz, D.B. The MCNPX Monte Carlo Radiation Transport Code. In *AIP Conference Proceedings*; American Institute of Physics: College Park, MD, USA, 2007; Volume 896, pp. 81–90. [CrossRef]
15. Şakar, E.; Özpolat, Ö.F.; Alım, B.; Sayyed, M.; Kurudirek, M. Phy-X/PSD: Development of a user friendly online software for calculation of parameters relevant to radiation shielding and dosimetry. *Radiat. Phys. Chem.* **2020**, *166*, 108496. [CrossRef]
16. Kebaili, I.; Boukhris, I.; Sayyed, M. Gamma-ray shielding properties of lead borovanadate glasses. *Ceram. Int.* **2020**, *46*, 19624–19628. [CrossRef]
17. Abdullah, M.S.; Alhuthali, A.; Kumar, M.; Sayyed, I.; Al-Hadeethi, Y. Investigations of Gamma Ray Shielding Properties of MoO_3 Modified P_2O_5-SiO_2-K_2O-MgO-CaO GLASSES. *Dig. J. Nanomater. Biostruct.* **2021**, *16*, 183–189.
18. Akkurt, I.; Tekin, H.O. Radiological Parameters for Bismuth Oxide Glasses Using Phy-X/PSD Software. *Emerg. Mater. Res.* **2020**, *9*, 1020–1027. [CrossRef]
19. Madelung, O.; Rössler, U.; Schulz, M. (Eds.) *II-VI and I-VII Compounds; Semimagnetic Compounds of Volume B41 'Semiconductors' of Landolt-Börnstein—Group III Condensed Matter*; Springer: Berlin/Heidelberg, Germany, 1999.
20. Martins, J.F.T.; Dos Santos, R.A.; Ferraz, C.D.M.; Oliveira, R.R.; Fiederle, M.; Amadeu, R.D.A.; Dos Santos, R.S.; Da Silva, T.L.B.; Hamada, M.M. Optimization of the HgI_2 Crystal Preparation for Application as a Radiation Semiconductor Detector. *Stud. Eng. Technol.* **2017**, *5*, 76–88. [CrossRef]
21. Agar, O. Study on gamma ray shielding performance of concretes doped with natural sepiolite mineral. *Radiochim. Acta* **2018**, *106*, 1009–1016. [CrossRef]
22. Tekin, H.O.; Kavaz, E.; Papachristodoulou, A.; Kamislioglu, M.; Agar, O.; Altunsoy Guclu, E.E.; Kilicoglu, O.; Sayyed, M.I. Characterization of SiO_2–PbO–CdO–Ga_2O_3 glasses for comprehensive nuclear shielding performance: Alpha, proton, gamma, neutron radiation. *Ceram. Int.* **2019**, *45*, 19206–19222. [CrossRef]
23. Sayyed, M.; Kumar, A.; Tekin, H.; Kaur, R.; Singh, M.; Agar, O.; Khandaker, M.U. Evaluation of gamma-ray and neutron shielding features of heavy metals doped Bi_2O_3-BaO-Na_2O-MgO-B_2O_3 glass systems. *Prog. Nucl. Energy* **2020**, *118*, 103118. [CrossRef]
24. Al-Hadeethi, Y.; Sayyed, M. Radiation attenuation properties of Bi_2O_3–Na_2O–V_2O_5–TiO_2–TeO_2 glass system using Phy-X/PSD software. *Ceram. Int.* **2020**, *46*, 4795–4800. [CrossRef]
25. Kumar, A.; Gaikwad, D.; Obaid, S.S.; Tekin, H.; Agar, O.; Sayyed, M. Experimental studies and Monte Carlo simulations on gamma ray shielding competence of (30+x)PbO 10WO_3 10Na_2O−10MgO–(40−x)B_2O_3 glasses. *Prog. Nucl. Energy* **2020**, *119*, 103047. [CrossRef]

26. Prabhu, N.; Hegde, V.; Sayyed, M.; Agar, O.; Kamath, S.D. Investigations on structural and radiation shielding properties of Er3+ doped zinc bismuth borate glasses. *Mater. Chem. Phys.* **2019**, *230*, 267–276. [CrossRef]

27. Obaid, S.S.; Sayyed, M.; Gaikwad, D.; Pawar, P. Attenuation coefficients and exposure buildup factor of some rocks for gamma ray shielding applications. *Radiat. Phys. Chem.* **2018**, *148*, 86–94. [CrossRef]

28. Tekin, H.; Kavaz, E.; Altunsoy, E.; Kilicoglu, O.; Agar, O.; Erguzel, T.; Sayyed, M. An extensive investigation on gamma-ray and neutron attenuation parameters of cobalt oxide and nickel oxide substituted bioactive glasses. *Ceram. Int.* **2019**, *45*, 9934–9949. [CrossRef]

29. Kavaz, E.; Tekin, H.; Agar, O.; Altunsoy, E.; Kilicoglu, O.; Kamislioglu, M.; Abuzaid, M.; Sayyed, M. The Mass stopping power/projected range and nuclear shielding behaviors of barium bismuth borate glasses and influence of cerium oxide. *Ceram. Int.* **2019**, *45*, 15348–15357. [CrossRef]

30. Manjunatha, H. A study of gamma attenuation parameters in poly methyl methacrylate and Kapton. *Radiat. Phys. Chem.* **2017**, *137*, 254–259. [CrossRef]

31. Devillers, M. Lifetime of electrons in metals at room temperature. *Solid State Commun.* **1984**, *49*, 1019–1022. [CrossRef]

32. Çelik, A.; Çevik, U.; Bacaksiz, E.; Çelik, N. Effective atomic numbers and electron densities of CuGaSe2 semiconductor in the energy range 6–511 keV. *X-Ray Spectrom.* **2008**, *37*, 490–494. [CrossRef]

33. Turner, J.E. *Atoms, Radiation and Radiation Protection*, 2nd ed.; John Wiley & Sons: New York, NY, USA, 1995.

34. Cember, H.; Turner, J.E. Introduction to Health Physics. Second Edition. *Phys. Today* **1984**, *37*, 78. [CrossRef]

35. Partridge, M.; Donovan, E.; Fenton, N.; Reise, S.; Blane, S. Clinical implementation of a computer controlled milling machine for compensating filter production. *Br. J. Radiol.* **1999**, *72*, 1099–1103. [CrossRef]

36. Sayyed, M.; Kaky, K.M.; Şakar, E.; Akbaba, U.; Taki, M.M.; Agar, O. Gamma radiation shielding investigations for selected germanate glasses. *J. Non-Cryst. Solids* **2019**, *512*, 33–40. [CrossRef]

37. Kurudirek, M. Heavy metal borate glasses: Potential use for radiation shielding. *J. Alloys Compd.* **2017**, *727*, 1227. [CrossRef]

38. Al-Hadeethi, Y.; Sayyed, M.; Agar, O. Ionizing photons attenuation characterization of quaternary tellurite–zinc–niobium–gadolinium glasses using Phy-X/PSD software. *J. Non-Cryst. Solids* **2020**, *538*, 120044. [CrossRef]

39. Bashter, I.I. Calculation of radiation attenuation coefficients for shielding concretes. *Ann. Nucl. Energy* **1997**, *24*, 1389–1401. [CrossRef]

40. Sabry, N.; Zahran, H.; Yousef, E.S.; Algarni, H.; Umar, A.; Albargi, H.B.; Yahia, I. Gamma-ray attenuation, fast neutron removal cross-section and build up factor of Cu2MnGe[S, Se, Te]4 semiconductor compounds: Novel approach. *Radiat. Phys. Chem.* **2021**, *179*, 109248. [CrossRef]

41. Cevik, U.; Balta, H.; Çelik, A.; Bacaksız, E. Determination of attenuation coefficients, thicknesses and effective atomic numbers for CuInSe$_2$ semiconductor. *Nucl. Instrum. Methods B* **2006**, *247*, 173–179. [CrossRef]

42. Elbashir, B.; Sayyed, M.; Dong, M.; Elmahroug, Y.; Lakshminarayana, G.; Kityk, I. Characterization of Bi_2O_3ZnO B_2O_3 and TeO_2ZnO CdO Li_2O V_2O_5 glass systems for shielding gamma radiation using MCNP5 and Geant4 codes. *J. Phys. Chem. Solids* **2019**, *126*, 112–123. [CrossRef]

43. Cevik, U.; Bacaksiz, E.; Damla, N.; Çelik, A. Effective atomic numbers and electron densities for CdSe and CdTe semiconductors. *Radiat. Meas.* **2008**, *43*, 1437–1442. [CrossRef]

44. Al-Buriahi, M.S.; Tonguc, B.T. Study on gamma-ray buildup factors of bismuth borate glasses. *Appl. Phys. A* **2019**, *125*, 482. [CrossRef]

45. Manohara, S.; Hanagodimath, S.; Gerward, L. Energy absorption buildup factors for thermoluminescent dosimetric materials and their tissue equivalence. *Radiat. Phys. Chem.* **2010**, *79*, 575. [CrossRef]

46. Sorenso James, A. Absorption-Edge Transmission Technique Using Ce-139 for Measurement of Stable Iodine Concentration. *J. Nucl. Med.* **1979**, *20*, 1286–1293.

47. Itami, T.; Mizuno, A. The Variation of Absorption Edges of X-Rays for Liquid Hg-Rb Alloys. *Mater. Trans.* **2008**, *49*, 2254–2258. [CrossRef]

48. Lakshminarayana, G.; Dong, M.G.; Al-Buriahi, M.S.; Kumar, A.; Lee, D.-E.; Yoon, J.; Park, T. B_2O_3–Bi_2O_3–TeO_2–BaO and TeO_2–Bi_2O_3–BaO glass systems: A comparative assessment of gamma-ray and fast and thermal neutron attenuation aspects. *Appl. Phys. A* **2020**, *126*, 1–18. [CrossRef]